Journal of the Iranian Chemical Society (2021) 18:13–27
https://doi.org/10.1007/s13738-020-02000-2

ORIGINAL PAPER

Facile synthesis of Ce-doped SnO_2 nanoparticles with enhanced performance for photocatalytic degradation of organic dye

Ameer Baig Ali Baig[1] · Vadamalar Rathinam[1] · Jayanthi Palaninathan[1]

Received: 23 March 2020 / Accepted: 7 July 2020 / Published online: 21 July 2020

Abstract

Cerium (Ce)-doped tin dioxide (SnO_2) nanoparticles (NPs) have been prepared by a facile hydrothermal coprecipitation route for photocatalytic decomposition of methyl orange (MO) dye. The as-obtained NPs were characterized using different physical methods. X-ray diffraction (XRD) analysis found a rutile-phase-like crystalline structure. X-ray photoelectron spectroscopy (XPS) revealed specific energies of 486.2 eV for Sn $3d_{3/2}$ and 497.4 eV for Sn $3d_{5/2}$ and confirmed an oxidation state of Sn^{4+}. With increasing Ce concentration (from 0% to 2% and 4%), the optical bandgap energy of the SnO_2 NPs reduced (3.4–3.1 eV), resulting in a red-shift that enhanced their photocatalytic activity. The 4% Ce:SnO_2 NPs exhibited superior photodegradation performance against MO organic dye, achieving 94.5% decomposition in 100 min under exposure to ultraviolet–visible (UV–Vis) light. Indeed, the photocatalytic efficiency of the 4% Ce:SnO_2 NPs was 4.9- and 2.44-fold higher than that of the bare SnO_2 and 2% Ce:SnO_2 NPs, respectively. This outstanding photodegradation efficacy of the as-obtained 4% Ce:SnO_2 NPs was due to the effective doping of Ce into the SnO_2 lattice, thus preventing the recombination and allowing the effective separation/migration of photoexcited charges (e^-/h^+). Furthermore, improved antibacterial activity against two bacteria was clearly observed when adding Ce dopant to the SnO_2 NPs.

Keywords Antibacterial activity · Ce-doped SnO_2 · Methyl orange dye · Nanoparticles · Photocatalysts

Introduction

The rapid worldwide phenomenon of industrialization and expansion, as well as increased population, has led to various problems related to human health and the environment [1, 2]. Water effluence occurs due to excessive use of pesticides, pharmaceutical excess, oils, and industrialized waste, among other sources. Dyes are mostly colored complexes such as methyl orange (MO) and industrial sewage, being released uncontrolled into water bodies [3], resulting in the release of large amounts of such non-biodegradable materials into the atmosphere. These effects can result in problems for all living beings as well as raising health-related concerns due to their toxic and carcinogenic nature, and posing an ecological risk and causing allergies and skin irritation, representing a danger to humans as well as aquatic biota [4–6]. Their removal from wastewater to achieve clean water has thus attracted great attention worldwide [7]. To achieve this, various treatment methods such as chemical oxidation, coagulation, filtration, precipitation, ion exchange, biosorption, adsorption, reverse osmosis, and photocatalytic decay have been developed [8]. However, for photocatalytic dye degradation, advanced oxidation processes (AOPs) such as the photo-Fenton, ozonation, and photolysis methods have been applied, whereas semiconductor-based photocatalysis has been considered to represent the most active process to address the increasing environmental crisis and energy shortage. Against this background, this approach represents an advanced, low-cost, and highly efficiency method that is also environmentally friendly, since it uses energy from light with the help of a photocatalyst to create highly reactive species that can finally achieve the photodegradation of the dye [9]. Such ecological concerns can be addressed by removing these organic dye impurities from wastewater by degradation into nontoxic complexes. To date, the narrow light response range and low quantum efficacy of semiconductor photocatalysts (PCs) have been crucial issues hindering their applications. A large number of PC materials are

✉ Ameer Baig Ali Baig
ameerramphysics@gmail.com

[1] PG and Research Department of Physics, Muthurangam Government Arts College (Autonomous), Vellore, Tamil Nadu 632 002, India

used at present, including Bi_2O_3, CeO_2, TiO_2, CuS, SnO_2, ZrO_2, and ZnO, being among the most important compounds used for the decolorization of organic dyes and other toxic substances [9–14].

SnO_2 is a potential and suitable wide-bandgap semiconductor that is related to the TiO_2 nanomaterials (NMs) that are already widely used as photocatalysts. Amongst these, SnO_2 is usually an *n*-type direct-bandgap (E_g ~ 3.6 eV) material that is generally used in the fields of Li-ion/sodium-ion batteries, solar cells, photoelectrochemical applications, supercapacitors, gas sensors, and photocatalysis, owing to its outstanding physical and chemical robustness, abundance, high photosensitivity, robust oxidizing power, exciton binding energy of ~ 130 MeV, high electron mobility (~ 200 $cm^2\ V^{-1}\ s^{-1}$), low resistivity, superb optical and electrical properties, low cost, and nontoxicity [15, 16]. Unfortunately, the photocatalytic action of bare SnO_2 is inadequate due to its wide bandgap which results in poor utilization of solar radiation. Also, SnO_2 can only use UV light, which represents < 6% of solar energy; attempts have thus been made to adjust SnO_2 to use visible light, which represents ~ 45% of natural sunlight [17]. In contrast, the high recombination rate of photoexcited (e^-/h^+) pairs in bare SnO_2 also limits its various catalytic applications. To resolve this difficulty, several modification schemes, including (co) doping with metal or nonmetal ions, and coupling of metal oxides such as SnO_2 with α-Fe_2O_3, MnO_2, WO_3, CuO, or noble metals such as Ce, La, Au, Ag, and Pd, have been explored [18–20]. Moreover, it has been found that doping of different rare-earth ions into metal NPs not only alters their optical properties but also greatly enhances their photocatalytic efficacy [21]. Such investigations of Ce-doped SnO_2 NPs have revealed their potent catalytic activity, probably being due to the catalytic effect of Ce^{3+}/Ce^{4+} ions. Ce^{3+}/Ce^{4+} ions typically have a diameter larger than that of Sn^{4+} ions (with ionic radii of Sn^{4+} and Ce^{3+}/Ce^{4+} of 0. 7 and 0.114/0.92 Å, respectively). Additionally, the application of Ce doping with low-valence cations that can act as electron (e^-) acceptors and (e^-/h^+) traps can not only hinder the recombination of photoexcited (e^-/h^+) pairs but also leave the oxygen vacancies (V_O) in the host lattice, ensuring an enhancement of the photocatalytic action to degrade organic impurities [22, 23]. This overview reveals that doping of Ce ions into the SnO_2 lattice may create large amounts of V_O vacancies without altering the crystal structure, causing charge imbalance, or distortion, thus opening up more application scenarios. Besides, there are several ways to make SnO_2 NPs, including sol–gel, chemical precipitation, solvothermal, thermal calcination microwave, and hydrothermal synthesis methods. Hydrothermal synthesis is an appropriate method for making NPs in a single step, yielding ultrafine powder in a short time and at low cost with good energy efficiency.

The work presented herein focuses on the effect of doping Ce at different concentrations (0%, 2%, and 4%) into SnO_2 (Ce:SnO_2) NPs made by a facile hydrothermal precipitation approach. The prepared NPs were characterized by XRD analysis, Fourier-transform infrared (FT-IR) spectroscopy, high-resolution scanning electron microscopy (HR-SEM) with energy-dispersive X-ray spectroscopy (EDX), high-resolution transmission electron microscopy (HR-TEM), XPS, UV–Vis diffuse reflectance spectroscopy (DRS), and photoluminescence (PL) techniques. In this work, photodecomposition of methyl orange (MO) as a model pollutant was also studied in the presence of Ce:SnO_2 NPs as a photocatalyst under UV–Vis light, and the response is discussed in detail. The results of this study may thus deliver new prospects for clean, low-cost materials for use in energy generation and environmental applications.

Experimental details

Materials and reagents

Sodium hydroxide (NaOH), tin(IV) chloride ($SnCl_4{\cdot}5H_2O$) pentahydrate, ethylenediamine tetraacetic acid (EDTA-2Na), 1,4-benzoquinone (BQ), isopropanol (IPA), and absolute ethanol (CH_3CH_2OH) were obtained from SDFCL Chemical Reagent Co., Pvt. Ltd. India. Cerium(III) nitrate hexahydrate [$Ce(NO_3)_3{\cdot}6H_2O$] was procured from Himedia Chemical Lab. Pvt. Ltd. Methylene blue ($C_{16}H_{18}ClN_3S$) dye was obtained from SD Fine Chemical Co., Pvt. Ltd. The aforementioned materials were used as precursors. Also, all the ingredients used in this work were of analytical grade (AR) and used without further purification. Deionized water (DI) was used throughout the experimental processes.

Preparation of Ce:SnO_2 NPs

Ce:SnO_2 NPs with appropriate amounts (0%, 2%, and 4%) of cerium (Ce) dopant were prepared from Sn in DI water as starting materials via a facile hydrothermal chemical precipitation approach [15]. Typically, 0.1 M $SnCl_4{\cdot}5H_2O$ was used as a template to organize the SnO_2 NPs. The $SnCl_4{\cdot}5H_2O$ was dissolved in HCl/DI water mixture solution (1:4 with total volume of 50 mL). To this, NaOH solution (1.25 M NaOH diluted in 20 mL DI water) was added dropwise under vigorous magnetic stirring to increase the pH value to ~ 10 to form precipitates. To achieve a water-soluble Ce dopant, $Ce(NO_3)_3{\cdot}6H_2O$ at different concentrations of 0, 2, or 4 wt% was added to the same mixture solution. The resulting solution was kept under constant stirring for 6 h to obtain a uniform homogeneous solution. It was then transferred to a Teflon-lined stainless-steel autoclave and kept at 160 °C for 24 h, then left to cool naturally to room temperature. The

resulting product was washed extensively using DI water and ethanol to remove Cl^- ions by testing the residual liquid, then dried in a hot oven at 70 °C overnight [24]. The residual product was gently powdered into fine powder NPs using an agate mortar to obtain 2% and 4% Ce:SnO_2 NPs for further characterization. An equivalent procedure was used to synthesize undoped/pristine SnO_2 NPs without addition of cerium.

Characterization techniques

The crystalline phases, structure, and size of the as-obtained samples was studied by XRD analysis using a Bruker Tensor device with a monochromatic Cu K_α radiation source in the range from 10° to 80°. FT-IR spectroscopy was carried out using a PerkinElmer RX-1 spectrophotometer to evaluate the surface functional groups. HRSEM was used to study the surface morphology, the particle size of the NPs, as well as their elemental composition in %, and hence confirm the successful doping of Ce into the nanostructures, using a Hitachi S-3000 H microscope equipped with an EDX unit. The deep morphology, particle size, and crystalline structure of the 4% Ce:SnO_2 NPs were studied by HR-TEM (JEOL, Japan) using selected-area electron diffraction (SAED) analysis. XPS was carried out using a PHI 5000 VersaProbe III-ULVAC surface analysis instrument to determine the chemical composition and binding energy states of the as-obtained samples. The optical properties and bandgap energy (E_g) were determined by UV–Vis DRS (PerkinElmer UV/Vis Lambda 19) in the wavelength from 200 to 800 nm. Room-temperature photoluminescence (PL) spectra were studied using a Horiba IHR-550 with a Xe lamp in the excitation range of ~ 309–315 nm.

Photocatalytic experiments

The photodecomposition of MO aqueous (20 ppm) colorant (100 mL; 10 mg L^{-1}) solution by the as-obtained Ce:SnO_2 NP photocatalysts was studied under UV–Vis light illumination from a high-pressure mercury lamp (300 W) in a steady ambient environment using 10 mg of each PC sample. Before irradiation, stirring was applied in the dark for 30 min to achieve adsorption–desorption equilibrium between the MO organic pollutant and catalyst surface, then the mix was exposed to light illumination [25]. To maintain a constant temperature, a quartz photoreactor with a water flow jacket was placed in a steel vessel with a magnetic stirrer. After a certain time (20 min), aliquots of 2.0 mL were extracted from the photoreactor and centrifuged to eliminate the catalyst. The absorption of the MO dye (λ_{max} of ~ 464 nm) solution was recorded after photocatalytic degradation for fixed time intervals by using a UV–Vis spectrophotometer (UV-3600, Shimadzu). The dominant trapping mechanism was investigated by adding IPA, BQ, and EDTA as scavengers for hydroxyl ($^{\cdot}OH^-$) and superoxide radicals ($^{\cdot}O^{2-}$) and holes (h^+), respectively. The recyclability of the material was investigated by carrying out four iterations to determine the robustness of the as-obtained photocatalysts.

Evaluation of antibacterial activity

The antibacterial action of the as-synthesized Ce:SnO_2 NPs was confirmed against *Escherichia coli* as a Gram-negative (G^-) and *Staphylococcus aureus* as a Gram-positive (G^+) infective bacterial strain using the agar-well diffusion method with addition of Mueller–Hinton agar for bacteriological culture [26]. Each well containing nutrient agar was carefully loaded with 50 µL of the obtained bare or Ce-doped SnO_2 mixed solution using a sterilized tool. The cultures were then placed in an incubator shaker for 37 °C at 24 h to study their evolution. Likewise, the evolution of a negative control containing only dimethyl sulfoxide (DMSO) was also studied. After the incubation period, the diameter of the zone of inhibition (ZOI) that formed in each well was measured and expressed as its mean ± standard deviation.

Results and discussion

Structural and functional group analysis

The crystalline structure and phase content of the 0%, 2%, and 4% Ce:SnO_2 samples were established by XRD analysis as shown in Fig. 1. The clear diffraction peaks revealed a tetragonal rutile-like phase of the SnO_2 nanostructure, in good agreement with standard Joint Committee on Powder Diffraction Standards (JCPDS) card

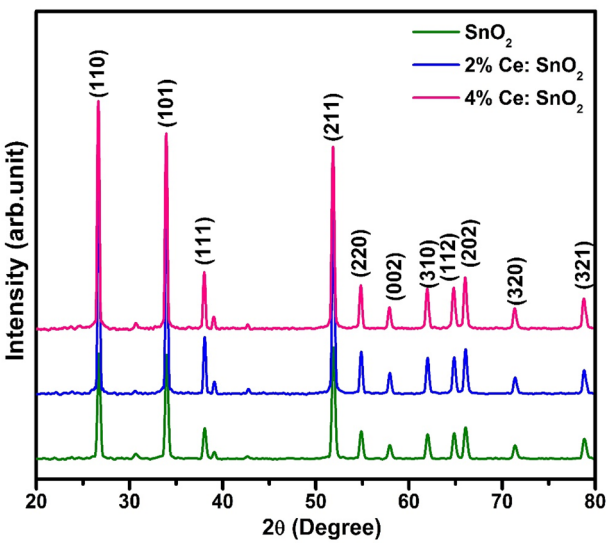

Fig. 1 Powder XRD patterns of as-prepared samples

no. 41-1445, indicating the highly crystalline nature of the as-obtained NPs [27]. For the 2% and 4% Ce:SnO_2 NP samples, the diffraction peaks were nearly the same as those obtained for the bare SnO_2, with no minor impurity phases being detected; i.e., peaks corresponding to Ce or CeO phase were not observable. For the Ce:SnO_2 samples, it can thus be speculated that specific cerium oxides formed of Ce–Sn–O solid solutions with SnO_2 were present, since no other species were observed in their structure. It is thus likely that the Ce^{3+} ions entered the matrix of the SnO_2 NPs to form a Ce–Sn–O solid solution, since the radius of Ce^{4+} (0.92 Å) is not much greater than that of Sn^{4+} (0.7 Å). The average crystalline size of the as-obtained samples was estimated by using the Debye–Scherrer formula $D = 0.89\,\lambda/\beta\cos\theta$ [28]. The results revealed that the 4% Ce:SnO_2 sample had a smaller crystalline size (~ 24.7 nm) than the 2% Ce:SnO_2 (~ 27.5 nm) or SnO_2 NP (29.3 nm) samples (Table 1). The crystallinity of the as-obtained samples was clearly affected by doping Ce into the SnO_2 host lattice, besides prompting defects in the system that hindered crystal growth. Moreover, such a smaller crystallite size would enhance the surface-to-volume ratio and oxygen vacancies (V_O), thereby improving the photocatalytic activity of the material [29].

FT-IR spectroscopy was applied to determine the characteristic molecular vibrations of the as-obtained samples, as shown in Fig. 2. A broad absorption peak appeared at about 3310–3500 cm^{-1}, in agreement with the bending vibrations of surface-absorbed water (H_2O) molecules, corresponding to the O–H stretching vibration modes of hydroxyl (–OH) groups [30]. The vibrational modes observed at 1370 and 2975 cm^{-1} agree with C–H bending modes which may be due to trace organic solvent impurities. The molecular stretching vibrations in the range of 560–730 cm^{-1} correspond to the major Sn–O–Sn and/or Ce–O modes, or the asymmetric stretching vibration of tin–hydroxyl (Sn–OH) at 1655 cm^{-1} in the effective bridging groups of SnO_2. The spectra show slight changes in the band intensities due to the effect of the Ce dopant on the SnO_2 host lattice [31]. The Ce–O bond indicates effective substitution of Sn by Ce in the SnO_2 crystal phase, beyond which no further absorption bands were observed [32] (Table 2).

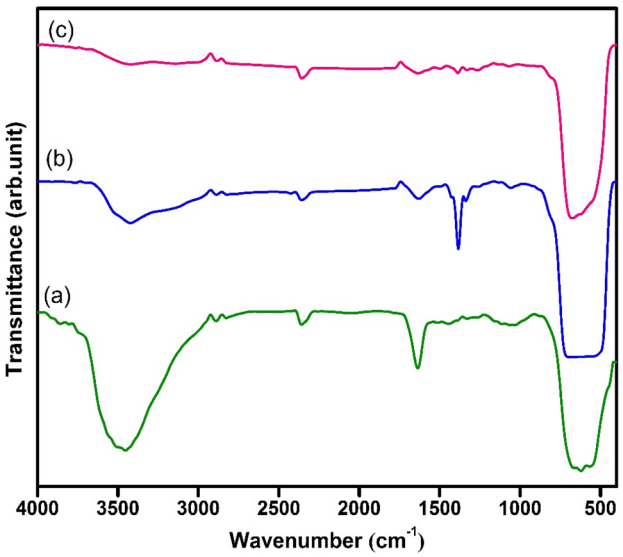

Fig. 2 FT-IR spectra of (a) SnO_2, (b) 2% Ce-doped SnO_2, and (c) 4% Ce-doped SnO_2 NPs

Surface morphology and elemental composition

The surface morphology and microstructure of the bare and 4% Ce:SnO_2 NPs were studied by HR-SEM. As seen in Fig. 3a, the bare SnO_2 sample showed a moderately monodispersed spherical morphology. As seen in Fig. 3b, c, the 4% Ce:SnO_2 NP sample exhibited less aggregation and a monodispersed spherical morphology [33, 34]. Figure 5a, b shows HRTEM images and (Fig. 5b, inset) a SAED pattern of the as-prepared 4% Ce:SnO_2 NPs, indicating nanosized crystallites but with a certain amount of agglomeration and monodisperse irregularly shaped NPs, which might be due to surface strain and interaction forces [35]. Moreover, the respective *hkl* planes of SnO_2 NMs were calculated, revealing an interplanar spacing (*d*) of 0.326 nm, which is in good agreement with the (110) crystal plane of tetragonal rutile phase of SnO_2. Lattice fringes of the samples were observed in different directions, indicating that the NPs were randomly oriented, thus confirming the crystalline nature of the sample [36]. This morphology and crystalline phase of the as-obtained photocatalyst will play an important role in enhancing its photocatalytic action [37]. The results mentioned above confirm the results of the XRD analysis. The

Table 1 Significant parameters of as-synthesized nanoparticles

S. no.	Sample	Average crystallite size (nm)	Bandgap (eV)	Degradation efficiency (%)	First-order kinetics (R^2)
1.	SnO_2 NPs	29.3	3.41	34.8	0.9885
2.	2% Ce-doped SnO_2 NPs	27.5	3.22	65.3	0.9754
3.	4% Ce-doped SnO_2 NPs	24.7	3.12	94.5	0.9783

Table 2 Comparison of the photodegradation rate (%) of MO dye under UV–Vis illumination with previously reported nanomaterial samples

S. no.	Photocatalyst	Dye	Irradiation time (min)	Degradation efficiency (%)	Refs.
1.	Coral SnO_2	MO	240	~50	[54]
2.	Eu-doped SnO_2	MO	210	~90	[46]
3.	ZnO/SnO_2	MB	240	~90	[4]
4.	$SnO_2/ZnO/TiO_2$	MO	240	~26	[55]
5.	TiO_2/Fe_2O_3	MO	150	~98	[56]
6.	ZnO/Cu_2O	MO	180	~70	[57]
7.	Ni-doped ZnO	MO	150	~79	[58]
8.	$Sn–SnO_2$	MB	180	~85	[59]
9.	SnO_2	MB	240	~91	[60]
10.	4% Ce-doped SnO_2	MO	180	~89.6	Current work

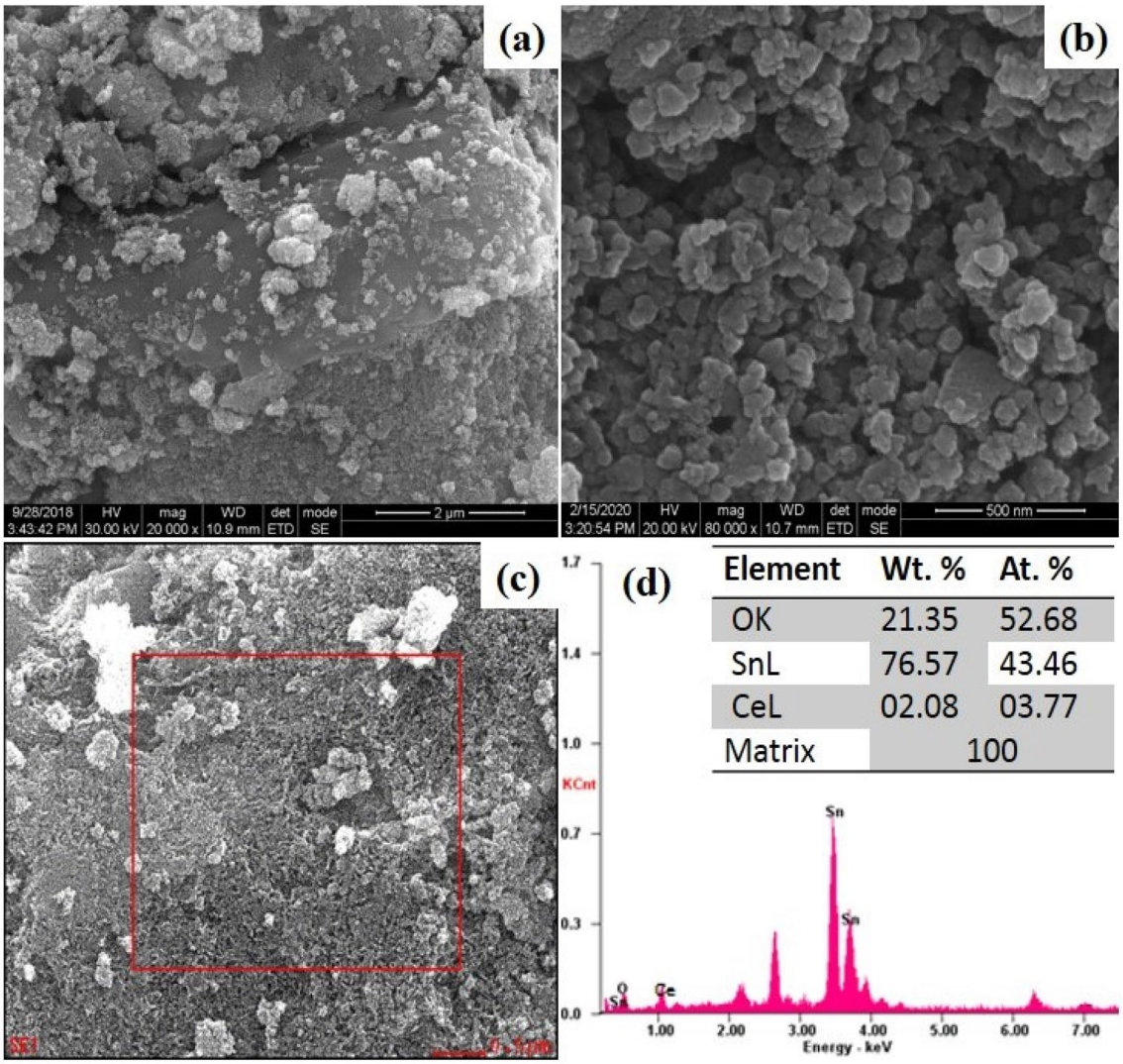

Fig. 3 FE-SEM images of **a** bare SnO_2 and **b**, **c** 4% Ce-doped SnO_2 NPs, with **d** EDAX spectra of 4% Ce-doped SnO_2 NPs

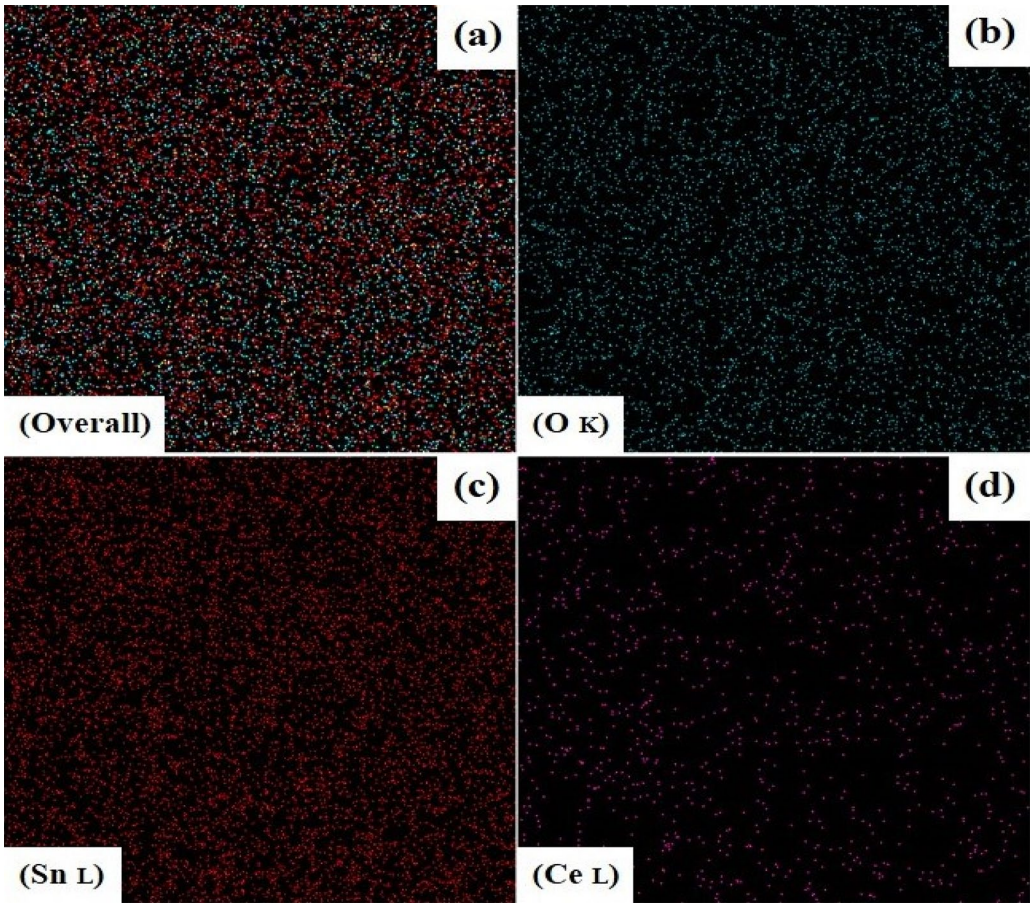

Fig. 4 EDAX elemental mapping of **a**–**d** 4% Ce-doped SnO_2 NPs

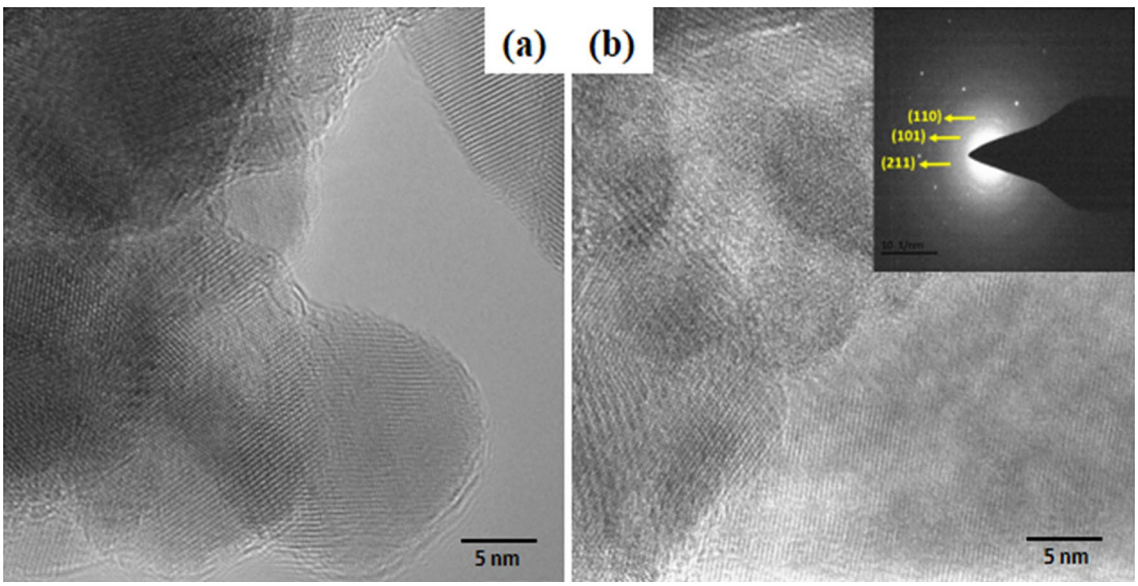

Fig. 5 **a** HR-TEM and **b** corresponding SAED pattern of 4% Ce-doped SnO_2 NPs

EDAX mapping results also confirmed the chemical configuration and elemental composition of the as-obtained 4% Ce:SnO_2 NP sample [33], being composed of tin (Sn), cerium (Ce), and oxygen (O) elements (Figs. 3d, 4a–d) distributed uniformly through the sample without other elements as also shown by the XPS results (Fig. 5).

Chemical composition by XPS

The high-resolution XPS spectrum of the 4% Ce:SnO_2 NPs is shown in Fig. 6a–c, showing binding energies of O 1*s*, Sn 3*d*, and Ce 3*d* in the core-level spectra at 531.1, 486.3, and 887.3 eV, respectively, with no trace of any other elements. In the high-resolution spectra, two strong and separated peaks were observed at 486.2 for Sn $3d_{5/2}$ and 497.4 eV for Sn $3d_{3/2}$; this spin–orbit splitting energy confirms an Sn^{4+} valence oxidation state in the rutile tetragonal structure that is characteristic of the SnO_2 nanostructure. This result indicates that the oxidation state of the SnO_2 NPs can be attributed to the Sn^{4+} region as usual [38]. To assess the valence state of the Ce ions, the Ce 3*d* core spectrum was measured to determine the presence and nature of the dopant by Gaussian deconvolution. The results revealed two main peaks at binding energy of 886.9 and 893.6 eV (Fig. 6c), corresponding to the dopant for the Ce^{4+} $3d_{5/2}$ peak and Ce^{3+} $3d_{3/2}$ for the surface of the SnO_2 lattice doped with Ce metal ions in the as-obtained NPs. The presence of Ce^{4+} and Ce^{3+} in the SnO_2 indicates a charge modification that will produce oxygen vacancies (V_O) in the host crystal lattice. The single asymmetric signal in the O 1*s* core-level spectrum

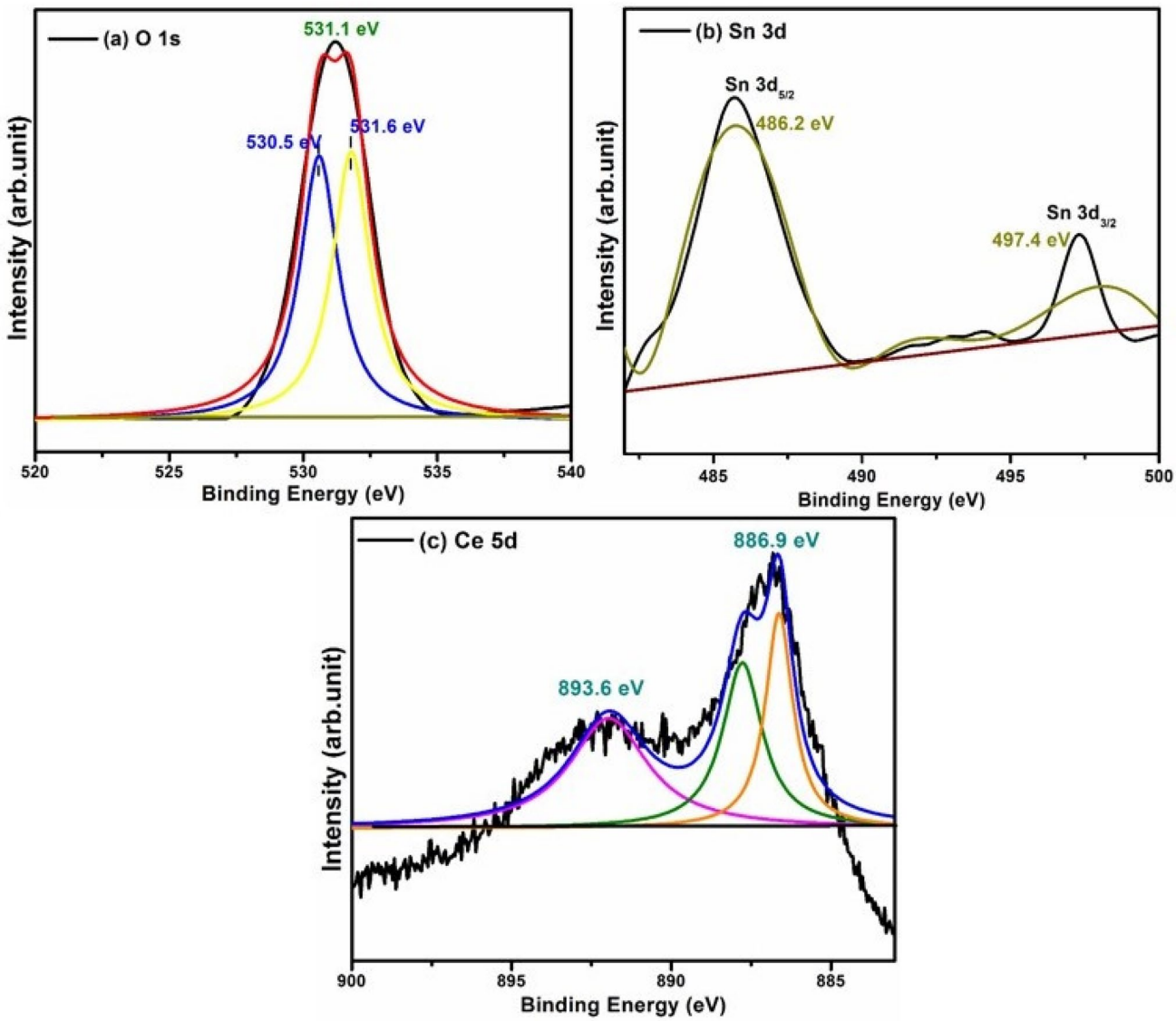

Fig. 6 XPS core-level spectra of O 1*s*, Sn 3*d*, and Ce 5*d* of Ce:SnO_2 sample

was deconvoluted into three curves, fit at 530.5, 531, and 531.6 eV, respectively [37]. The O 1*s* spectrum was thus related to lattice oxygen, oxygen–metal bonding, and the valence of chemisorbed oxygen, also corresponding to the binding energy of Sn^{4+}–O and O–H (hydroxyl) bonds [36]. In contrast, the formation of V_O in the NPs was evidenced by the survey spectrum and the inclusion of Ce ions, which are larger than Sn^{4+} in the metallic state. The inclusion of such a large amount of V_O should enhance the photocatalytic activity of the Ce:SnO_2 NPs by reducing the recombination rate of e^-/h^+ pairs. This confirms the effective doping of Ce into the SnO_2 NPs, in good agreement with the XRD and EDAX results described above.

Optical absorption and photoluminescence properties

The UV–Vis DRS spectra of the as-obtained 0%, 2%, and 4% Ce-doped SnO_2 NP samples in the range from 200 to 800 nm are shown in Fig. 7a. The absorption edge moved to longer wavelength with increasing Ce concentration (2% and 4%) with respect to the bare SnO_2 NPs, which can be ascribed to the electronic transition from the valence band (VB) to conduction band (CB) of SnO_2 [39]. The bandgap (E_g) energy of the as-produced NPs was estimated using the Tauc model $(\alpha h\nu)^2 = A(h\nu - E_g)$, where α, $h\nu$, E_g, and A are the absorption coefficient, incident photon energy, energy gap, and proportionality constant, respectively. The exponent n takes a fixed value of 2 in the case of a dominant indirect allowable transition. Figure 7b shows the plots of $(\alpha h\nu)^2$ versus $(h\nu)$ for the as-obtained samples, revealing bandgap values of 3.4, 3.21, and 3.11 eV, respectively. This variation in the bandgap values of the 0%, 2%, and 4% Ce-doped SnO_2 PCs (3.4 to 3.11 eV) might be due to the SnO_2 samples. Nevertheless, the sample with 4% Ce doping exhibited a narrower bandgap of 3.11 eV and a red-shift, thus capturing more visible light and exhibiting enhanced photocatalytic degradation ability due to the incorporation of Ce dopant into the SnO_2 lattice [40]. The photoresponse of the 4% Ce:SnO_2 PCs is thus changed from the UV to visible range. Conversely, the introduction of the Ce dopant could result in the formation of more extrinsic defective energy levels in the bandgap of SnO_2, thus yielding new energy levels in the NPs [41]. Also, the bandgap narrowed as the Ce concentration was increased (2% and 4%), corresponding to the *sp–d* exchange between band electrons and localized *d* electrons of the Ce^{3+} ions with electronic states in the Sn^{4+} ions. The *s–d* exchange interaction lowers the conduction-band (CB) edge, but the virtual to *p–d* exchange interaction raises the valence-band (VB) edge, resulting in bandgap narrowing [42].

PL spectroscopy was used for a systematic study of the effectiveness of charge-carrier trapping and recombination of photoexcited electron–hole (e^-/h^+) pairs [43]. The PL spectra (Fig. 8) of the Ce:SnO_2 NPs were measured at room atmosphere under exposure to intense wide violet emission with a major peak centered at ~ 422 nm. The observed reduction in the peak intensity can be attributed to defect centers, weaker trapped states in the energy gap, radiative recombination of photoexcited (e^-/h^+), in-plane oxygen vacancies (V_o), and surface defects caused by the insertion of Ce^{4+}/Ce^{3+} ions into the SnO_2 lattice. The interaction between these Sn^{4+} interstitials and the V_O vacancies resulted in

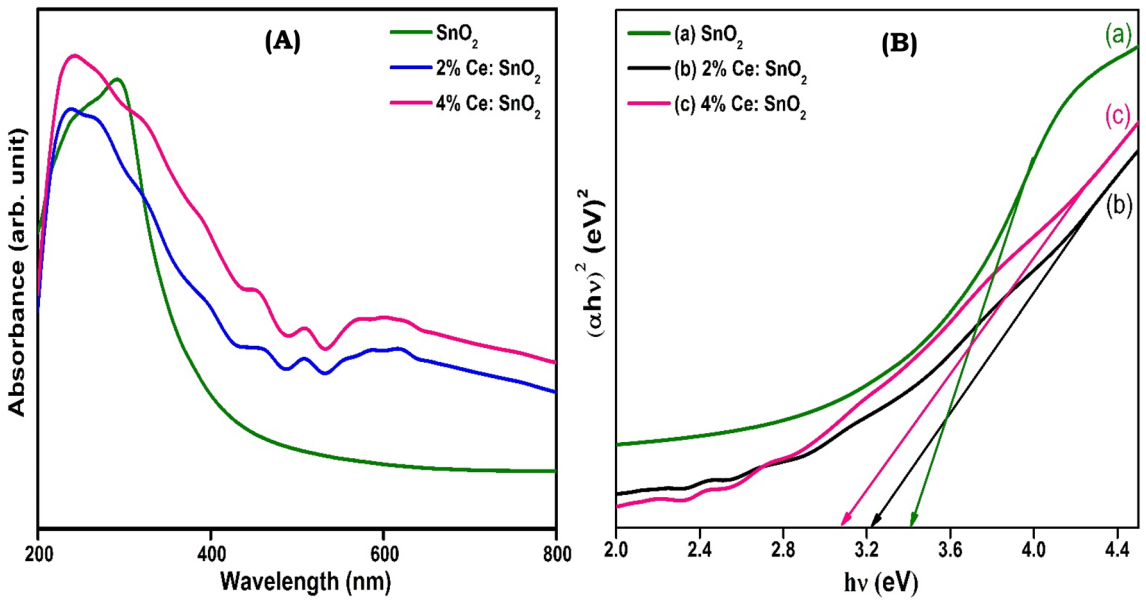

Fig. 7 **A** UV–Vis DRS spectra. **B** Bandgap values of as-obtained NPs

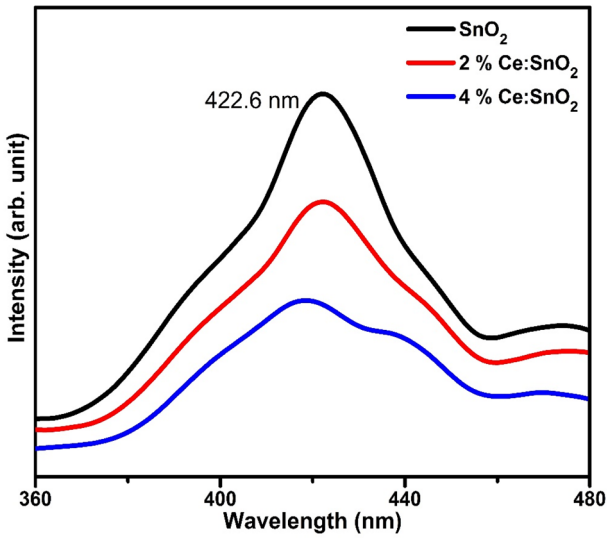

Fig. 8 Room-temperature PL spectra of as-obtained NPs

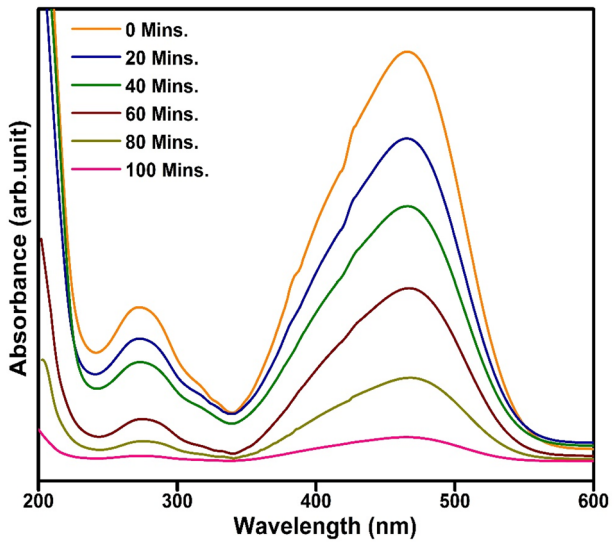

Fig. 9 UV–Vis absorption spectra during degradation of MO dye in presence of 4% Ce-doped SnO_2 NPs

sufficient trapping and metastable energy levels, causing the main PL emission [44]. These results confirm the enhanced photocatalytic activity of these semiconductor PCs.

Photocatalytic activity

The photocatalytic activity of the 0%, 2%, and 4% Ce-doped SnO_2 PCs were studied and compared based on the decomposition of MO as a model organic pollutant under UV–Vis illumination. The time-dependent UV–Vis spectra of the aqueous MO dye solution in the presence of 4% Ce:SnO_2 PCs at equal time steps of 20 min are shown in Fig. 9. These results indicate that the intensity of the peaks corresponding to MO dye progressively decreased with increasing reaction time [45]. When illuminated, the 4% Ce:SnO_2 PCs exhibited much greater photocatalytic ability than the bare SnO_2 PCs due to the doping effect of the Ce ions and the reduction of the bandgap energy. The negligible response observed for the control sample without catalyst addition corresponding to the photolysis of the MO colorant revealed almost no photocatalytic action [44]. Figure 10a, b shows the degradation efficacy of the as-obtained 0%, 2%, and 4% Ce-doped SnO_2 PCs under illumination quantified as C/C_0, where C and C_0 are the instantaneous and initial absorption of MO dye, respectively [46]. These results show that the 4% Ce:SnO_2 PCs displayed enhanced photocatalytic action compared with the other as-obtained photocatalytic samples [47]. In particular, the Ce:SnO_2 PCs with a doping content of 4% could photocatalytically degrade 94.5% of the MO dye after a degradation time of 100 min. Also, 34.8% and 65.3% of the MO dye could be photocatalytically degraded in the presence of the 0% and 2% Ce:SnO_2 PCs in identical conditions. According to these results, the degradation of the MO dye was confirmed to follow a pseudo-first-order kinetic response, corresponding to an abridged Langmuir–Hinshelwood model with a rate equation of $\ln(C_0/C) = kt$, where k is the first-order rate constant and t is the reaction time [48]. As shown in Fig. 11a, the 4% Ce:SnO_2 PCs exhibited the maximum rate constant (0.5681 min^{-1}) as well as improved photocatalytic activity which was 4.9-fold that observed for bare SnO_2 NPs under the same conditions [49–51]. These results indicate that the photocatalytic action and kinetic rate coefficient of the Ce:SnO_2 PCs with different Ce^+ concentrations lay in the following order: 4% Ce:SnO_2 > 2% Ce:SnO_2 > SnO_2 PCs. These results confirm that the ideal Ce doping concentration was 4% to achieve the strongest photocatalytic action for the decomposition of MO dye under UV–Vis illumination of the Ce:SnO_2 PCs. Below this optimal doping concentration of 4%, the photocatalytic activity increased with increasing dopant content due to the increasing number of trapping sites that become available, finally reaching the optimum doping concentration of Ce in the SnO_2 matrix [45, 52, 53]. Comparison with previous reports [4, 46, 54–60] reveals the greater photocatalytic activity of the current Ce-doped SnO_2 NPs.

Analysis of photocatalytic robustness

Repeatability and constancy are essential characteristics of PCs from a practical point of view, in addition to enhancing the photocatalytic action in order to achieve catalysts with greater degradation efficiency [61–63]. To study its reusability, the 4% Ce:SnO_2 PC was used four times for photocatalysis under similar conditions, as shown in Fig. 11b. After each cycle, the catalyst was recovered by centrifugation and

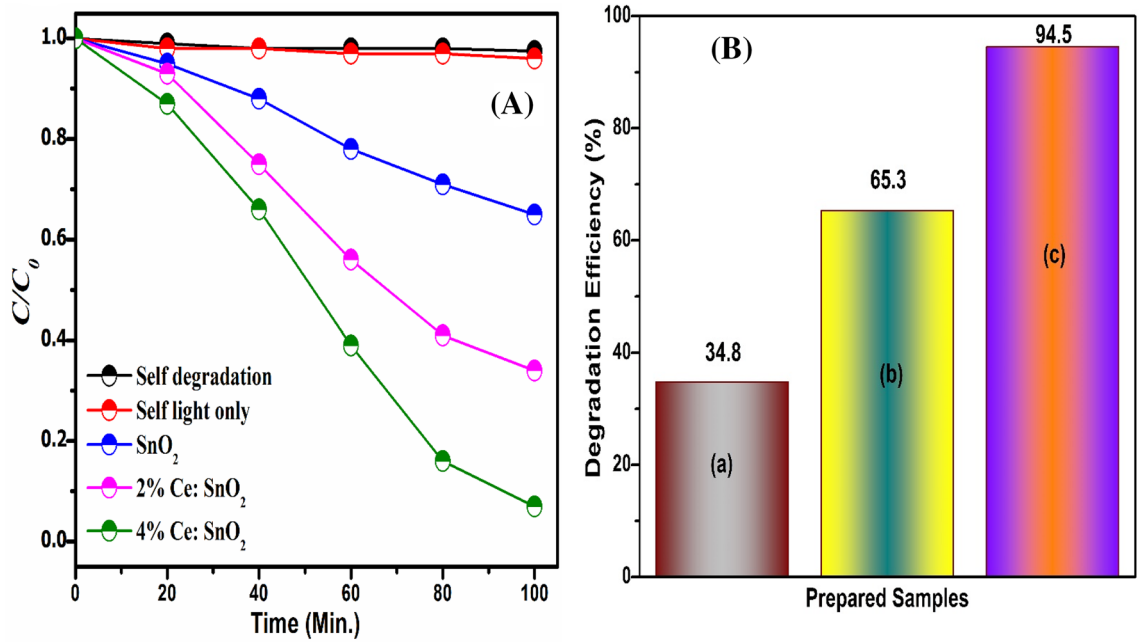

Fig. 10 **A** Photocatalytic degradation of MO dye and **B** degradation efficiency of as-prepared NPs under UV–Vis illumination

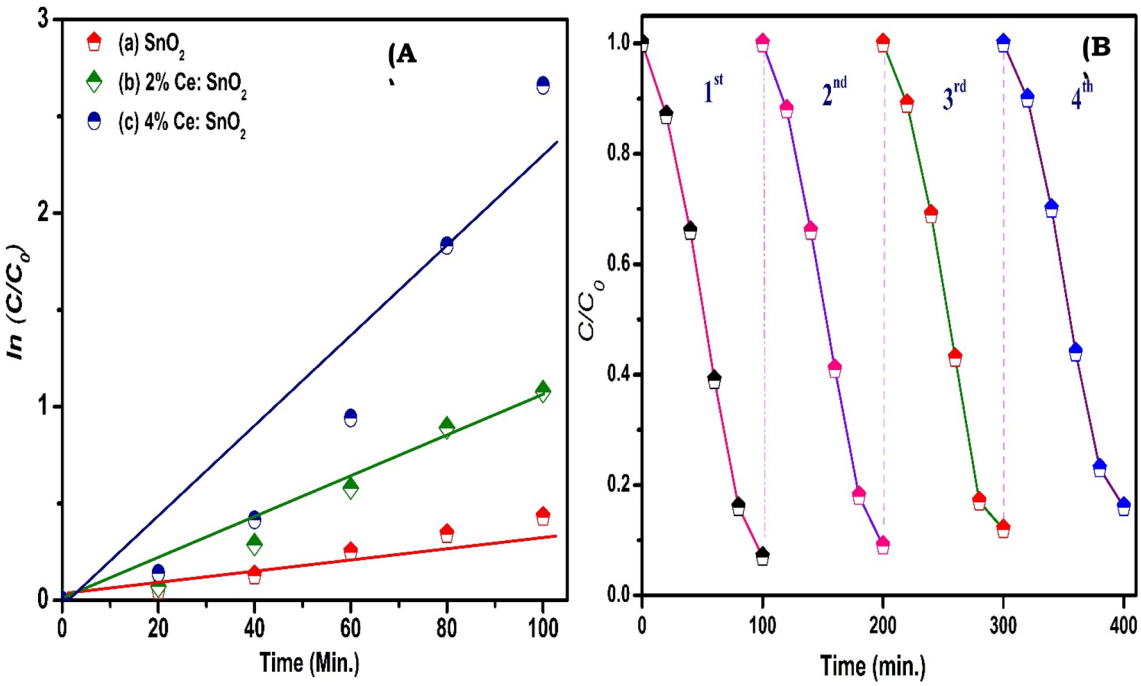

Fig. 11 **A** Pseudo-first-order kinetic plot of as-obtained NPs. **B** Four recycles of degradation of MO dye over 4% Ce-doped SnO_2 NPs

washed with DI water until the supernatant became clear. The washed photocatalyst sample was dried at 60 °C for 5 h then reused for degradation of MO dye solution. The photocatalyst exhibited only minor loss of action after four recycles (94.5–89%), which might be attributed mostly to incomplete recovery and loss through the washing process [64]. Likewise, the XRD pattern and FTIR spectra of the 4% Ce:SnO_2 PC before and after use in the photocatalytic reaction are shown in Fig. 12a, b, revealing no apparent changes; this confirms the robust nature of the Ce:SnO_2 NPs

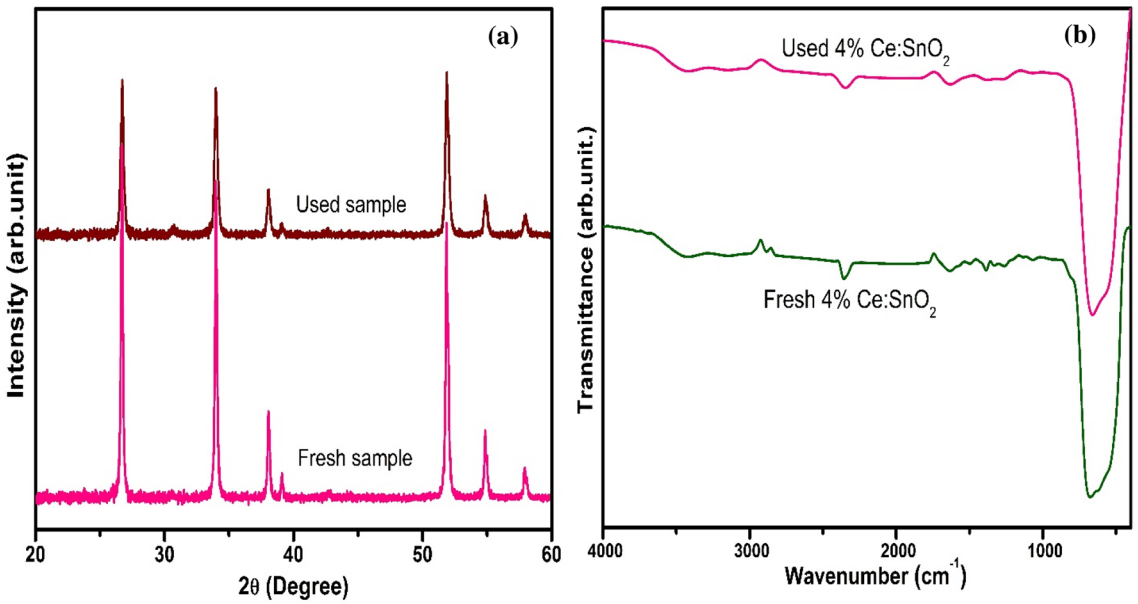

Fig. 12 **a** XRD pattern and **b** FTIR spectra of 4% Ce:SnO_2 NPs in fresh condition and after use for photocatalysis reaction

[65, 66]. These results confirm that such 4% Ce:SnO_2 PCs would exhibit effective reusability and robustness as high-performance photocatalysts for the decomposition of MO dye in wastewater.

Trapping study and possible photocatalytic mechanism

Radical scavenging was applied to study the nature of the different energetic species taking part in the photocatalytic degradation of the MO dye in wastewater. In this study, IPA, BQ, and EDTA were applied, being frequently used as radical scavengers of $^{\cdot}OH^{-}$, $^{\cdot}O^{2-}$, and h^{+}, respectively [67]. When BQ was added, the efficacy of MO dye degradation in 100 min decreased noticeably from 91% to 25.6%, as shown in Fig. 12, indicating that superoxide radical anions ($^{\cdot}O_2^{-}$) play a critical role in the photodegradation process. Additionally, the results show that $^{\cdot}OH^{-}$ also played a substantial role, because the degradation efficiency of the MO solution dropped to 68% after addition of IPA. Also, when EDTA was added, the MO degradation efficiency declined to 74.5%, indicating that h^{+} plays a clear but minor role [45] (Fig. 13).

Reactive oxygen species (ROSs) are the main components responsible for the photodegradation response in the photocatalytic process. When the Ce:SnO_2 catalyst is treated with light, it is excited by the photons. When the incident photon energy is equal to or above the bandgap energy (E_g), electrons (e^{-}) can be promoted from the VB to CB while a similar number of holes (h^{+}) are formed in the VB, resulting in the formation of (e^{-}/h^{+}) pairs [63, 68, 69]. The h^{+} in the VB react with H_2O or hydroxide ions (OH^{-}) adsorbed

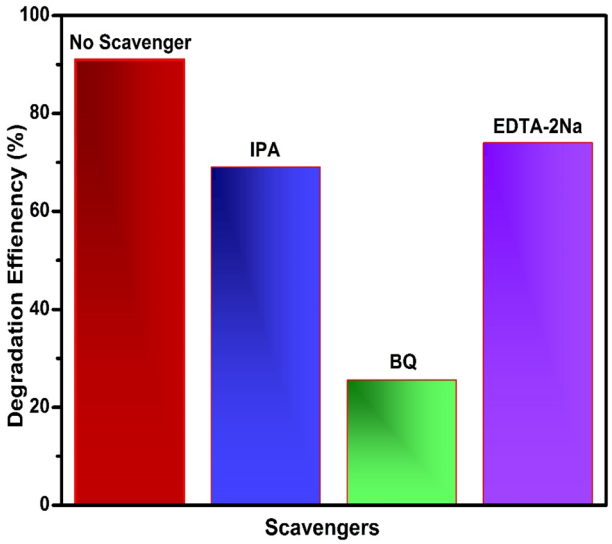

Fig. 13 Effects of different scavengers on MO dye photodegradation in presence of 4% Ce:SnO_2 sample

on the surface of the obtained NPs to yield hydroxyl radicals ($^{\cdot}OH^{-}$). The (e^{-}) in the CB can be reduced by scavenged O_2 released from H_2O to create superoxide radical anions ($^{\cdot}O_2^{-}$) and finally hydrogen peroxide (H_2O_2) [54, 70]. The decreased bandgap and PL intensity are related to the charge separation efficacy and might arise due to the solid interface interaction on the Ce:SnO_2 PCs, thus decreasing the recombination of (e^{-}/h^{+}) pairs, while the surface characteristics of the SnO_2 will greatly enhance the photoabsorption and thus increase the photocatalytic action. The

enhanced photocatalytic activity of the Ce:SnO_2 NPs could also be attributed to their smaller crystallite size, which will cause water (H_2O) and chemisorbed hydroxyl groups on the surface of the PCs to react with photoexcited holes to form hydroxyl radicals ($^{\cdot}OH^{-}$). Furthermore, the transfer/separation of the photoexcited (e^{-}/h^{+}) at the interface of the as-prepared Ce:SnO_2 NPs will also be related to the enhanced recombination rate [71, 72]. This would further extend the lifetime of the charge carriers due to the Ce^{+} ions, thereby enhancing the photocatalytic activity of the samples under illumination. A potential mechanism for the photodegradation of MO dye using the Ce:SnO_2 NPs under UV–Vis illumination is depicted schematically in Fig. 14. Note that these two radicals, viz. $\dot{O}_2^{-}$ and $^{\cdot}OH^{-}$, are prevailing oxidizing agents which can react immediately with the organic molecules of the MO colorant on the surface of the photocatalyst, resulting in effective photodegradation, forming CO_2 and H_2O as byproducts [73, 74]. Based on the results presented above, a probable mechanism can be proposed [72] based on the sequence expressed in Eqs. 1–6:

$$\mathrm{Ce}:\mathrm{SnO_2} + \mathrm{MO\ Dye} + h\nu \rightarrow \mathrm{Ce{:}SnO_2} + \mathrm{MO\ dye} + \left(e^{-}(CB) + h^{+}(VB)\right) \quad (1)$$

$$\mathrm{Dye} + \mathrm{OH} \rightarrow \mathrm{OH}^{\cdot -} + \text{degradation byproducts} \quad (2)$$

$$\mathrm{Dye} + \mathrm{O_2} \rightarrow \mathrm{O_2^{\cdot -}} + \text{degradation byproducts} \quad (3)$$

$$\mathrm{O_2} \rightarrow e^{-}(\mathrm{CB}) + 2h^{+} + \mathrm{H_2O_2} \quad (4)$$

$$\mathrm{Dye} + e^{-}\,(\mathrm{CB}) \rightarrow \text{reduction products} \quad (5)$$

$$\mathrm{Dye} + h^{+}\,(\mathrm{VB}) \rightarrow \text{oxidative products.} \quad (6)$$

Antibacterial activity

The antibacterial activity of the Ce:SnO_2 NPs was studied by the agar well diffusion method using *S. aureus* and *E. coli* as typical microorganisms. Considering the objective of developing a new group of antibiotics, the antibacterial action was studied against both *S. aureus* and *E. coli* bacteria to determine the ability of such materials to kill bacteria [75]. The ZOI results presented in Fig. 15 confirm that the antibacterial action of the 0%, 2%, and 4% Ce-doped SnO_2 PCs was higher against *S. aureus* (G^{+}) than *E. coli* (G^{-}), since G^{-} bacteria have a double-wall membrane which provides further protection to the bacteria from oxygen species. The antibacterial effect increased with increasing concentration of SnO_2 NPs, and the microbial ZOI of the as-obtained NPs

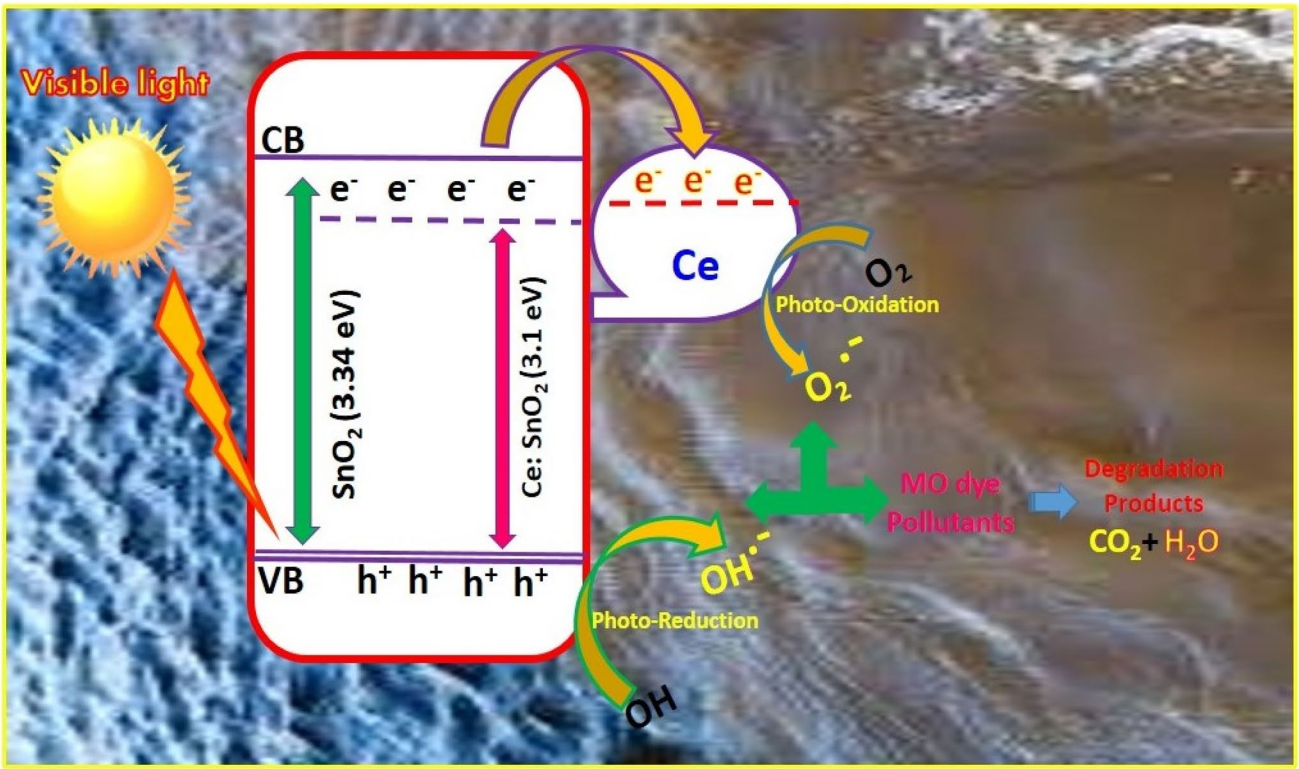

Fig. 14 Potential mechanism for MO dye photodegradation over 4% Ce:SnO_2 NPs

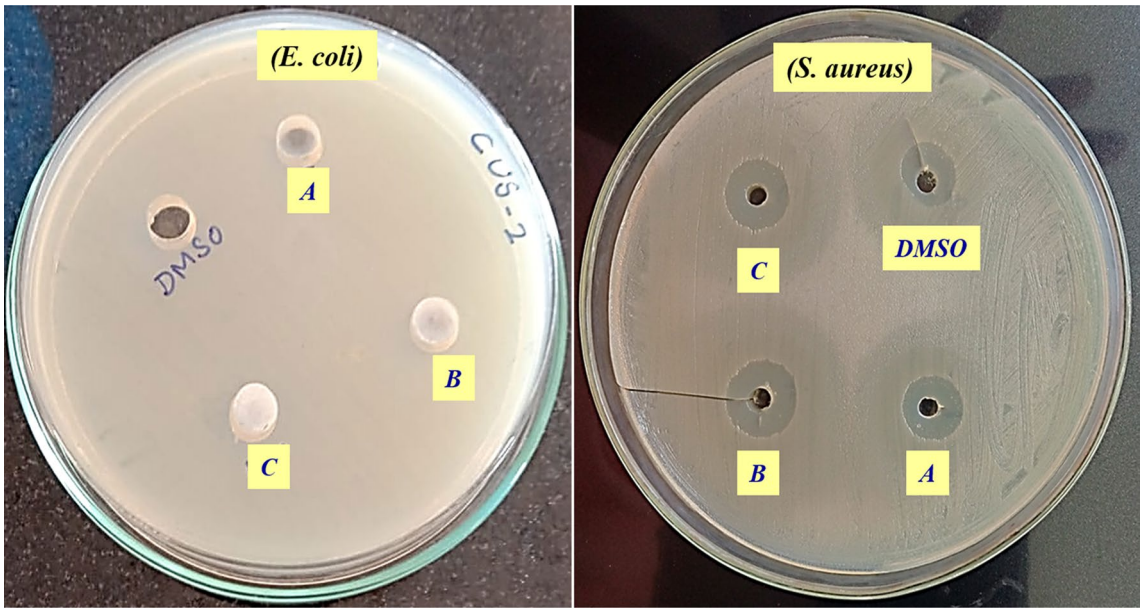

Fig. 15 Zone of inhibition results for the (A) bare, (B) 2%, and (C) 4% Ce:SnO_2 NPs towards *E. coli* and *S. aureus* bacteria

Table 3 Zone of inhibition (ZOI) results showing the antibacterial activity of as-prepared NPs

S. no.	Microorganism	Zone of inhibition range (mm)	
		E. coli	*S. aureus*
1.	SnO_2	4 ± 0.5	7 ± 0.5
2.	2% Ce:SnO_2 NPs	4 ± 0.5	7 ± 1
3.	4% Ce:SnO_2 NPs	5 ± 1	9 ± 1

are presented in Table 3. In the current case, the 4% Ce:SnO_2 PCs exhibited higher antibacterial action with a mean ZOI of 9 ± 1 mm against *S. aureus* and 5 ± 1 mm against *E. coli* bacterial. It is also clear from these results that the as-obtained 4% Ce:SnO_2 PCs exhibited good action against both bacteria with respect to the standard antibiotic DMSO. When Ce^+ was doped into the SnO_2, interstitials might be released from the lattice rather than from lattice sites, and could thus contribute efficiently to the observed antibacterial ability [76, 77]. The observed variation in the activity against both types of bacteria can also be explained based on the chemical configuration of the Ce with respect to the cell surface. The cell wall of G^- bacteria is different from that of G^+ bacteria due to the presence of an exterior membrane that covers the peptidoglycan layer. The positively charged surface of the metal NPs is attracted to the oppositely charged surface of the bacteria, which could result in the development of a bactericidal effect [26]. Another cause of the greater antibacterial activity with the Ce dopant is the increased surface area due to the particle size; i.e., the antibacterial effect will be greater for smaller crystallite size. According to the results of the different mechanisms presented to described antibacterial actions, the ROS species H_2O_2 is the most deadly species, exhibiting easy dispersion into bacteria owing to the surface of the bacteria and/or the weaker electrostatic interface between the Sn^{4+} and Ce^{3+} ions and the cell membrane, resulting in inhibition by the NPs and eventually cell death [78]. These results confirm that the as-obtained NPs have potential as effective antibiotic agents.

Conclusions

Ce-doped SnO_2 nanoparticles with different Ce contents were manufactured using a simple hydrothermal approach via a cost-effective scheme. The successful substitution of Ce^+ into the SnO_2 NPs was confirmed by characterization using techniques such as XRD analysis, HR-SEM, HRTEM, XPS, FT-IR spectroscopy, UV DRS, and PL spectroscopy. The obtained XPS and EDX spectra confirmed the presence of Sn, O, and Ce elements. PL measurements revealed that the emission intensity steadily declined with increasing Ce doping. The degradation of MO dye in the presence of the 4% Ce:SnO_2 photocatalyst revealed its superior photocatalytic action, achieving 94.5% impurity removal in 100 min, which was 4.9 times greater than that obtained when using the bare SnO_2 under UV–Vis illumination. Moreover, the $\dot{O}_2^-$ radical species played a prevailing role in the MO dye photodegradation process. Reusability experiments using the 4% Ce:SnO_2 PC confirmed its long-term robustness over four test cycles. The enhanced photocatalytic performance can

be attributed to the combined effects of the reduced crystallite size, decreased bandgap, separation/transfer efficiency, suppressed recombination of photoexcited (e^-/h^+) pairs, amplification of the visible-light absorption, and increased oxygen vacancies (V_O) in the SnO_2 nanostructures after Ce doping. The results of this study confirm the potential of this new material with the optimal dopant concentration with increased effectiveness and outstanding stability for photocatalytic purification of wastewater with associated environmental benefits.

References

1. J. Mazloom, F.E. Ghodsi, H. Golmojdeh, J. Alloys Compd. **639**, 393 (2015)
2. N. Manjula, G. Selvan, J. Mater. Sci.: Mater. Electron. **28**, 15056 (2017)
3. S. Koner, A. Pal, A. Adak, Desalination **276**, 142 (2011)
4. M.M. Rashad, A.A. Ismail, I. Osama, I.A. Ibrahim, A.-H.T. Kandil, Arab. J. Chem. **7**, 71 (2014)
5. S. Nath, S.K. Ghosh, S. Panigahi, T. Thundat, T. Pal, Langmuir **20**, 7880 (2004)
6. A.K. Das, S. Saha, A. Pal, S.K. Maji, J. Environ. Sci. Health Part A **44**, 896 (2009)
7. L. Ran, D. Zhao, X. Gao, L. Yin, CrystEngComm **17**, 4225 (2015)
8. H. Chen, L. Ding, W. Sun, Q. Jiang, J. Hu, J. Li, RSC Adv. **5**, 56401 (2015)
9. T. Karimi, A. Haghighatzadeh, Bull. Mater. Sci. **42**, 158 (2019)
10. J. Singh, T. Dutta, K.-H. Kim, M. Rawat, P. Samddar, P. Kumar, J. Nanobiotechnol. **16**, 84 (2018)
11. A.K. Sinha, M. Basu, M. Pradhan, S. Sarkar, T. Pal, Chem. Eur. J. **16**, 7865 (2010)
12. S. Asaithambi, P. Sakthivel, M. Karuppaiah, R. Murugan, R. Yuvakkumar, G. Ravi, J. Electron. Mater. **48**, 2183 (2019)
13. M. Basu, A.K. Sinha, M. Pradhan, S. Sarkar, Y. Negishi, T. Pal, Environ. Sci. Technol. **44**, 6313 (2010)
14. S. Jana, S. Pande, A.K. Sinha, T. Pal, Inorg. Chem. **47**, 5558 (2008)
15. M. Kandasamy, A. Seetharaman, D. Sivasubramanian, A. Nithya, K. Jothivenkatachalam, N. Maheswari, M. Gopalan, S. Dillibabu, A. Eftekhari, ACS Appl. Nano Mater. **1**, 5823 (2018)
16. F. Dumitrache, I.P. Morjan, E. Dutu, I. Morjan, C.T. Fleaca, M. Scarisoreanu, A. Ilie, M. Dumitru, C. Mihailescu, A. Smarandache, G. Prodan, Beilstein J. Nanotechnol. **10**, 9 (2019)
17. S. Sagadevan, Z.Z. Chowdhury, M.R. Bin Johan, F.A. Aziz, L.S. Roselin, J. Podder, J.A. Lett, R. Selvin, J. Nanosci. Nanotechnol. **19**, 7139 (2019)
18. P. Mahamallik, S. Saha, A. Pal, Chem. Eng. J. **276**, 155 (2015)
19. J.Z. Marinho, L.F. de Paula, E. Longo, A.O.T. Patrocinio, R.C. Lima, SN Appl. Sci. **1**, 359 (2019)
20. C. Sahoo, A. Gupta, A. Pal, Dyes Pigm. **66**, 189 (2005)
21. A. Adak, M. Bandyopadhyay, A. Pal, Dyes Pigm. **69**, 245 (2006)
22. V. Kumar, Bhawna, S.K. Yadav, A. Gupta, B. Dwivedi, A. Kumar, P. Singh, K. Deori, ChemistrySelect **4**, 3722 (2019)
23. S. Wu, C. Li, W. Wei, H. Wang, Y. Zhu, Y. Song, J. Rare Earths **28**, 168 (2010)
24. L. Chu, F. Duo, M. Zhang, Z. Wu, Y. Sun, C. Wang, S. Dong, J. Sun, Colloids Surf. A **589**, 124416 (2020)
25. J.R. Sunkara, S.M. Botsa, Chem. Afr. **2**, 635 (2019)
26. R. Dobrucka, J. Dlugaszewska, M. Kaczmarek, Inorg. Nanomet. Chem. **48**, 367 (2018)
27. D. Chen, S. Huang, R. Huang, Q. Zhang, T.-T. Le, E. Cheng, Z. Hu, Z. Chen, J. Alloys Compd. **788**, 929 (2019)
28. S. Jayapandi, S. Premkumar, D. Lakshmi, P. Packiyaraj, K. Balaji Viswanath, P. Sivaraj, K. Anitha, J. Mater. Sci. Mater. Electron. **30**, 8479 (2019)
29. B. Babu, R. Koutavarapu, V.V.N. Harish, J. Shim, K. Yoo, Ceram. Int. **45**, 5743 (2019)
30. R. Mani, K. Vivekanandan, N.P. Subiramaniyam, J. Mater. Sci.: Mater. Electron. **28**, 13846 (2017)
31. D. Selleswari, P. Meena, D. Mangalaraj, J. Iran. Chem. Soc. **16**, 1291 (2019)
32. M. Singh, J. Singh, M. Rawat, J. Sharma, P.P. Singh, J. Mater. Sci.: Mater. Electron. **30**, 13389 (2019)
33. A. Ahmed, M. Naseem Siddique, U. Alam, T. Ali, P. Tripathi, Appl. Surf. Sci. **463**, 976 (2019)
34. C. Mondal, M. Ganguly, J. Pal, A. Roy, J. Jana, T. Pal, Langmuir **30**, 4157 (2014)
35. W. Ben Soltan, M.S. Lassoued, S. Ammar, T. Toupance, J. Mater. Sci. Mater. Electron. **28**, 15826 (2017)
36. P.A. Luque, O. Nava, C.A. Soto-Robles, M.J. Chinchillas-Chinchillas, H.E. Garrafa-Galvez, Y.A. Baez-Lopez, K.P. Valdez-Núñez, A.R. Vilchis-Nestor, A. Castro-Beltrán, Optik **206**, 164299 (2020)
37. B. Babu, A.N. Kadam, R.V.S.S.N. Ravikumar, C. Byon, J. Alloys Compd. **703**, 330 (2017)
38. X.-F. Wu, Y.-J. Wang, L.-J. Song, J.-Z. Su, J.-R. Zhang, Y.-N. Jia, J.-L. Shang, X.-W. Nian, C.-Y. Zhang, X.-G. Sun, J. Mater. Sci.: Mater. Electron. **30**, 14987 (2019)
39. M. Dhanalakshmi, K. Saravanakumar, S. Lakshmi Prabavathi, M. Abinaya, V. Muthuraj, J. Alloys Compd. **763**, 512 (2018)
40. D. Chen, S. Huang, R. Huang, Q. Zhang, T.-T. Le, E. Cheng, R. Yue, Z. Hu, Z. Chen, J. Hazard. Mater. **368**, 204 (2019)
41. S. Saha, J.M. Wang, A. Pal, Sep. Purif. Technol. **89**, 147 (2012)
42. W. Ben Haj Othmen, B. Sieber, H. Elhouichet, A. Addad, B. Gelloz, M. Moreau, S. Szunerits, R. Boukherroub, Mater. Sci. Semicond. Process. **77**, 31 (2018)
43. B. Babu, A.N. Kadam, G.T. Rao, S.-W. Lee, C. Byon, J. Shim, J. Lumin. **195**, 283 (2018)
44. X. Wang, M. Xu, L. Liu, Y. Cui, H. Geng, H. Zhao, B. Liang, J. Yang, J. Mater. Sci.: Mater. Electron. **30**, 16110 (2019)
45. J. Li, W. Hu, J. Zhong, J. Zeng, S. Huang, Z. Xiao, M. Li, Appl. Phys. A **116**, 2149 (2014)
46. T.T. Bhosale, A.R. Kuldeep, S.J. Pawar, B.S. Shirke, K.M. Garadkar, J. Mater. Sci.: Mater. Electron. **30**, 18927 (2019)
47. C. Sahoo, A.K. Gupta, A. Pal, Desalination **181**, 91 (2005)
48. A.K. Gupta, A. Pal, C. Sahoo, Dyes Pigm. **69**, 224 (2006)
49. J. Singh, N. Kaur, P. Kaur, S. Kaur, J. Kaur, P. Kukkar, V. Kumar, D. Kukkar, M. Rawat, Environ. Nanotechnol. Monit. Manag. **10**, 331 (2018)
50. B. Babu, M. Cho, C. Byon, J. Shim, J. Alloys Compd. **731**, 162 (2018)
51. S. Kundu, A. Pal, A.K. Dikshit, Sep. Purif. Technol. **44**, 121 (2005)
52. B. Liang, L. Zhang, W. Zhang, Ceram. Int. **45**, 8908 (2019)
53. S. Dutta, R. Sahoo, C. Ray, S. Sarkar, J. Jana, Y. Negishi, T. Pal, Dalton Trans. **44**, 193 (2015)
54. X. Wang, H. Fan, P. Ren, Colloids Surf. A **402**, 53 (2012)
55. G. Yang, Z. Yan, T. Xiao, Appl. Surf. Sci. **258**, 8704 (2012)
56. M. Gebrezgiabher, G. Gebreslassie, T. Gebretsadik, G. Yeabyo, F. Elemo, Y. Bayeh, M. Thomas, W. Linert, J. Compos. Sci. **3**, 75 (2019)
57. C. Xu, L. Cao, G. Su, W. Liu, H. Liu, Y. Yu, X. Qu, J. Hazard. Mater. **176**, 807 (2010)
58. J. Kaur, S. Singhal, Ceram. Int. **40**, 7417 (2014)
59. A.K. Sinha, M. Pradhan, S. Sarkar, T. Pal, Environ. Sci. Technol. **47**, 2339 (2013)

60. J. Singh, H. Kaur, D. Kukkar, V.K. Mukamia, S. Kumar, M. Rawat, Mater. Res. Express **6**, 115007 (2019)
61. M.T. Uddin, Y. Nicolas, C. Olivier, T. Toupance, L. Servant, M.M. Müller, H.-J. Kleebe, J. Ziegler, W. Jaegermann, Inorg. Chem. **51**, 7764 (2012)
62. M. Pradhan, A. Roy, A.K. Sinha, R. Sahoo, D. Deb, T. Pal, Dalton Trans. **44**, 1889 (2015)
63. S. Saha, A. Pal, S. Kundu, S. Basu, T. Pal, Langmuir **26**, 2885 (2010)
64. M. Kumar, A. Mehta, A. Mishra, J. Singh, M. Rawat, S. Basu, Mater. Lett. **215**, 121 (2018)
65. S. Selvarajan, P. Malathy, A. Suganthi, M. Rajarajan, J. Ind. Eng. Chem. **53**, 201 (2017)
66. R. Sahoo, A. Roy, C. Ray, C. Mondal, Y. Negishi, S.M. Yusuf, A. Pal, T. Pal, J. Phys. Chem. C **118**, 11485 (2014)
67. K. Vignesh, R. Hariharan, M. Rajarajan, A. Suganthi, Solid State Sci. **21**, 91 (2013)
68. N.K. Singh, S. Saha, A. Pal, Desalin. Water Treat. **56**, 1066 (2015)
69. T. Aditya, J. Jana, A. Pal, T. Pal, ACS Omega **3**, 9318 (2018)
70. W. Ben Soltan, S. Ammar, C. Olivier, T. Toupance, J. Alloys Compd. **729**, 638 (2017)
71. D. Madhan, P. Rajkumar, P. Rajeshwaran, A. Sivarajan, M. Sangeetha, Appl. Phys. A **120**, 463 (2015)
72. K. Sujatha, T. Seethalakshmi, A.P. Sudha, O.L. Shanmugasundaram, Nanostruct. Nanoobjects **18**, 100305 (2019)
73. J. Wang, H. Fan, H. Yu, J. Mater. Eng. Perform. **24**, 4260 (2015)
74. N.K. Singh, S. Saha, A. Pal, Desalin. Water Treat. **53**, 501 (2015)
75. A.T. Ravichandran, R. Karthick, A.R. Xavier, R. Chandramohan, S. Mantha, J. Mater. Sci.: Mater. Electron. **28**, 6643 (2017)
76. Z. Nasir, M. Shakir, R. Wahab, M. Shoeb, P. Alam, R.H. Khan, M. Mobin, Lutfullah, Int. J. Biol. Macromol. **94**, 554 (2017)
77. J. Jana, S.S. Gauri, M. Ganguly, S. Dey, T. Pal, Dalton Trans. **44**, 20692 (2015)
78. R. Pandiyan, S. Mahalingam, Y.-H. Ahn, J. Photochem. Photobiol. B **191**, 18 (2019)